Article

Cu(II)/polydopamine-modified glass fiber separators towards high-performance zinc-ion batteries

Fengcan Ma, Kaixuan Xie, Siheng Wu, Chi Zhang, Xiaodie Liao, and Qinghong Wang*

[1] School of Chemistry and Materials Science, Jiangsu Normal University, Xuzhou, Jiangsu 221116, China

* Correspondence: wangqh@jsnu.edu.cn

Abstract: Much attention has been attracted by aqueous zinc-ion batteries (ZIBs) due to the features of inherent safety, environmental compatibility, low cost and fantastic energy density. Nevertheless, chemical corrosion and dendrite growth occurring on Zn anode during the charge/discharge process usually cause the surface passivation and short circuit of cells, seriously hindering the development of AZIBs. To settle these problems, a Cu(II)/polydopamine modified glass fiber (Cu(II)-PDA/GF) is designed as separator. Due to the enhanced ionic conductivity of Cu(II) and PDA modified glass fiber separator, reversible zinc plating/striping is achieved in symmetric cells, which display long cycle life of over 1800 h at the current density of 1 mA cm^{-2} with the fixed capacity of 1 mAh cm^{-2}. Moreover, the assembled Zn//V_2O_5 cells using Cu(II)-PDA/GF separator also demonstrate improved capacity retention. The present study provides a simple separator modification strategy for high-performance and reliable AZIBs, which are conducive to energy storage devices.

Keywords: aqueous zinc ion batteries; separator; modification

1. Introduction

The excessive consumption of traditional fossil energy has aggravated the issues of energy shortage and environmental pollution. The exploitation and utilization of clean energy are severely limited by their defects of instability [1,2]. Therefore, developing reliable large-scale energy storage systems (ESSs) with the advantages of low cost, high energy density and high security is of great importance [3,4]. In recent years, aqueous rechargeable batteries, such as monovalent (K, Na) and multivalent (Mg, Ca, Zn, Al) ion batteries, have aroused much attention due to the features of nonflammability and abundant natural reserves [5-8]. Among these battery systems, zinc-ion batteries (ZIBs) are considered to be a good alternative of next-generation batteries due to the advantages of low redox potential (-0.76 V, vs. SHE) and high theoretical capacity (820 mAh g^{-1}) of Zn anode [8].

Unfortunately, undesirable dendrite growth and uncontrolled side reactions occurring on Zn anode could accelerate the failure of Zn metal battery. During the initial plating process, the random nucleation on Zn surface causes the nonuniform distribution of electric field, and leads to the vertically Zn growth on the protrusions, thus finally forming Zn dendrites [9], which may pierce the separator and cause short circuit of the cell. Moreover, hydrogen evolution causes exhaustion of electrolyte and chemical corrosion produces "dead Zn" which accelerate the failure of the cells [10].

To overcome these problems, many strategies have been developed, such as modifying zinc anode [11-17], implanting electrolyte additives [18-21], and employing polymer or hydrogel-based electrolytes [22-26]. So far, most study are concern about decoration of electrolytes and electrodes, while little research focuses on separators. As a crucial component of batteries, separator could regulate the ion diffusion and optimize the electrochemical kinetics of batteries during the charge-discharge process, which could lead to dendrite-free Zn deposition. The common separators are glass fiber (GF) or filter paper (FP), both of which possess good compatibility with aqueous electrolytes, but they are

Preprints (www.preprints.org) | NOT PEER-REVIEWED | Posted: 9 June 2023 doi:10.20944/preprints202306.0719.v1

chemically inactive. Therefore, separators are usually functionalized by chemically engineering or surface modification to improve the cycle stability of ZIBs. For example, Janus separators with good electrolyte wettability and high ionic conductivity can be realized by decorating vertical graphene carpet [27] or $Ti_3C_2T_x$ MXene [28] on one side of commercial GF separator to homogenize interfacial electric field and promote Zn nucleation kinetics. Moreover, the supramolecules with abundant polar groups [29] were also reported to prevent the accumulation of Zn^{2+} and suppress the Zn dendrites by modifying GF separator. In addition, during zinc ion electrodeposition, the cellulose/GO composite separator (CG) [30] achieved ultra-stable dendrite-free anode through crystal orientation regulation.

Inspired by above research, we have designed a multifunctional Cu^{2+} doped polydopamine modified GF (Cu(II)-PDA/GF) separator for high-performance ZIBs. Figure 1 schematically illustrates the Zn plating process in the cells with pristine GF and Cu(II)-PDA/GF separators. As shown in Figure 1a, inhomogeneous Zn nucleation takes place at the initial plating stage in the cell with pristine GF separator, which further leads to the growth of disordered Zn dendrites due to the wild 2D Zn^{2+} diffusion at the electrode/electrolyte interface. The as-formed Zn dendrites are inclined to cause the failure and short circuit of cells. In contrast, the abundant zincophilic active sites (amino, imino and hydroxyl) in the Cu(II)-PDA/GF separator could regulate the randomly scattered ion, and result in homogeneously distributed Zn^{2+} flux over the entire Zn anode, which therefore induce uniform Zn plating and lessen the growth of Zn dendrites. Moreover, the extraordinarily strong adhesion is expected to induce intimate interaction between electrodes and GF and relieve the local surface tension of Zn metal [31]. Interestingly, numerous of Cu^{2+} are encapsuled in the PDA modification layer via the metal-ligand band with the functional groups and could be preferentially deposited to form metal Cu layer on Zn anode, which also contributed to the uniform Zn deposition due to the good affinity with Zn atoms [32-34]. Based on above features, Cu(II)-PDA/GF separator enables the Zn metal symmetric cell with long cycle life of 1800 h at 1 mA cm^{-2} with the specific capacity of 1 mAh cm^{-2}. The Zn//V_2O_5 delivers high capacity of 202.3 mAh g^{-1} even after 1000 cycles at 2 A g^{-1}.

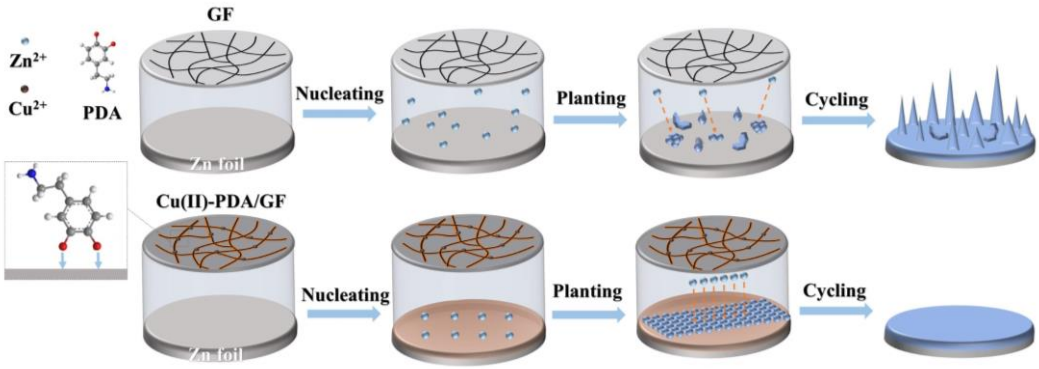

Figure 1. Schematics of Zn deposition with pristine GF and Cu(II)-PDA/GF separator.

2. Materials and Methods

2.1 Fabrication of the Cu(II)-PDA/GF separator： Typically, 1.2 g of Tris (Ph=8.5) and 0.40 g of dopamine hydrochloride (2 mg·mL^{-1}) were dissolved in 200 ml of deionized water under vigorous stirring. Then, 0.25 g of $CuSO_4 \cdot 5H_2O$ and 0.40 ml of H_2O_2 (19.6 mmol·L^{-1}) were added in above solution and stirred for 10 min. In addition, the GF separator was pre-wetted with absolute ethanol, and then completely submerged in the as-prepared solution for 40 min. Finally, the GF was extracted and washed with deionized water for three times and dried in the vacuum atmosphere at 50 °C for 12 h to obtain modified Cu(II)-PDA/GF separator.

2.2 Characterization: X-ray powder diffraction (XRD, Bruker-D8 Advance X-ray diffractometer, Cu Kα radiation), energy dispersive X-ray spectroscopy (EDS), and X-ray photoelectron spectroscopy (XPS, Thermo Fisher K-Alpha system) were performed for composition analysis. The scanning electron microscope (SEM, Hitachi SU-8010) were tested for the morphology detection.

 doi:10.20944/preprints202306.0719.v1

2.3 Electrochemical measurements: The CR2032 coin battery was assembled with 2 M $ZnSO_4$ as electrolyte and GF or Cu(II)-PDA/GF as separator. The V_2O5 cathode is prepared by mixing V_2O_5, superconducting C and polytetrafluoroethylene (PTFE) binder with a mass ratio of 7:2:1. Afterwards, the viscous material obtained by the above method was pressed into thin sheets with a mass load of ~2.0 mg cm^{-2}. The battery test system (LAND, CT2001A) is used to test the electrochemical performance of the battery. It was used for cyclic voltammetry (CV) and electrochemical impedance spectroscopy (EIS) tests on the CHI 660e electrochemical station.

3. Results and discussion

Dopamine readily self-polymerizes into PDA nanopolymers via an oxidation process, which can be deposited on the surface of various substrates to form functional coatings due to the super non-covalent/covalent bonding capability of catechol and quinone moieties. Herein, PDA nanopolymers are self-assembled on GF separator to regulate the zincophilic and ion transport properties via dipping GF in DA monomer solution with $CuSO_4/H_2O_2$ as a trigger [35]. As shown in Figure 2a and S1, after the infiltration process, the color of the GF separator changes from white to brown. SEM images shown in Figure 2a and 2b display that the modified Cu(II)-PDA/GF separator retains its original porous structure, which will facilitate the fast and full infiltration of electrolyte. High magnification SEM image further displays that the surface of GF is uniformly coated by polymeric PDA nanoparticles (Figure 2b). EDS mapping images also exhibit the even distribution of element Si, C, N and Cu, further confirming the successful coating of Cu(II)-doped PDA on GF (Figure 2c).

To investigate the chemical environment of the coating layer, XPS of the freshly prepared Cu(II)-PDA/GF was carried out. As shown in Figure 2d, typical peaks of Cu 2p, O 1s, N 1s, C 1s and Si 2p can be obviously observed from the XPS survey spectra, further verifying the successful modification of GF. The peaks located at 283.9 eV, 285.2 eV and 287.2 eV in the high-resolution XPS spectra of C1s can be indexed to C-H, C-N/C-O and C=O bond, respectively (Figure 2e). And that located at 399.0 eV and 400.3 eV in N 1s spectra is corresponding to the =NR and R_2N-H bond (Figure 2f). Notably, the obvious signals of Cu 2p located at 953 eV, 941.9 eV and 933.4 eV can be attributed to 2p1/2, 2p3/2 and satellite peaks of Cu^{2+} (Figure 2g), indicating that Cu^{2+} is trapped in the PDA layer due to the complexation reaction between Cu^{2+} and catechol groups. The introduction of Cu^{2+} could promote the polymerization of PDA [36]. XPS O1s peaks 533.4 ev, 532.1 ev, 531.2 ev and 530.1 ev correspond to O-H, C-O, C=O and Cu-O, respectively, further indicating the doping of Cu(II) in the PDA coating layer (Figure 2h). Based on above analysis, it can be confirmed that polymeric Cu(II)-PDA layer is successfully constructed on GF separator.

Ionic conductivity is an important indicator for the selection of a separator. EIS test of the stainless steel//stainless steel cells are carried out to evaluate the ion conductivity of pristine GF separator and Cu(II)-PDA/GF separator. As shown in Figure S2, the bulk resistance R_b at the high frequency intercept of the Nyquist plot is 0.97 Ω for Cu(II)-PDA/GF separator and 1.32 Ω for pristine GF. The ionic conductivity is calculated to be 89.01 mS cm^{-1} and 65.82 mS cm^{-1} for Cu(II)-PDA/GF and pristine GF, respectively, indicating significant improved ion conductivity of the modified GF.

 doi:10.20944/preprints202306.0719.v1

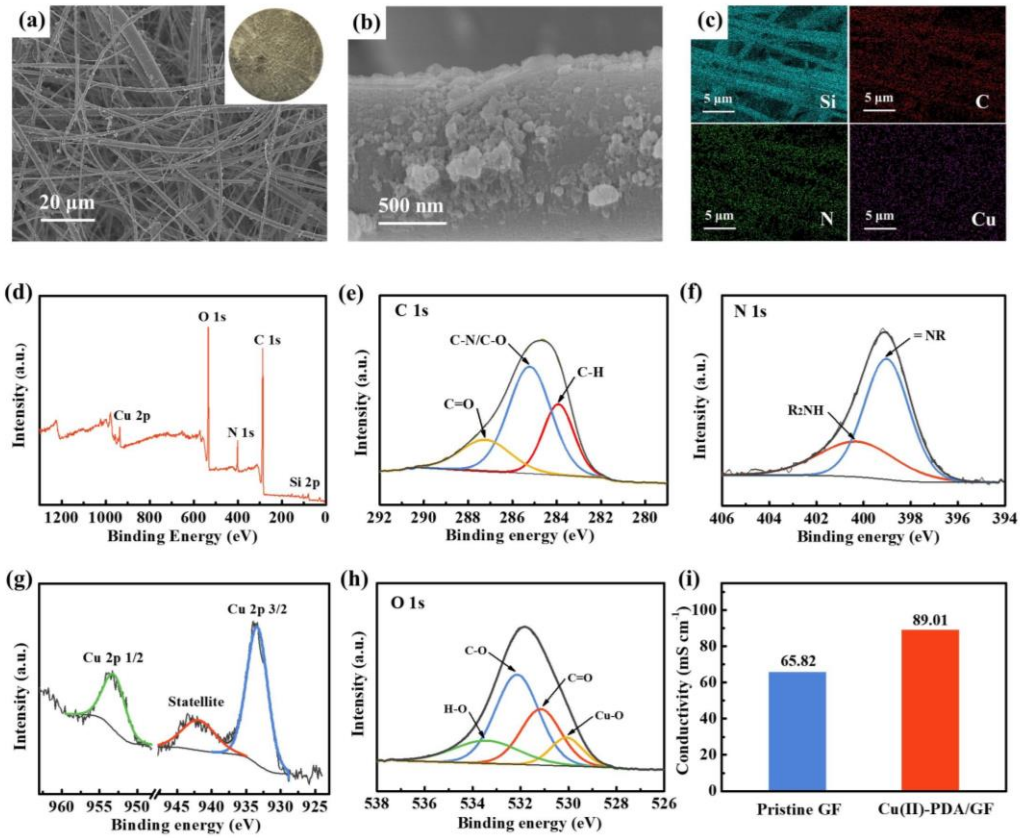

Figure 2. (a, b) SEM images of Cu(II)-PDA/GF separator; Insert in (a) is the photo of Cu(II)-PDA/GF. (c) EDS images of Cu(II)-PDA/GF separator; XPS survey spectra of Cu(II)-PDA/GF separator: (d) Full survey XPS spectra; High-resolution XPS spectra of (e) C 1s, (f) N 1s, (g) Cu 2p and (h) O 1s; (i) Ion conductivity of pristine GF and Cu(II)-PDA/GF separator.

To elucidate the effect of Cu(II)-PDA/GF separator on the electrochemical behavior of Zn anode, morphology evolution of the Zn anode during the deposition process at 1 mA cm^{-2} was characterized by SEM. As shown in Figure 3a, messy dendrite growth starts to occur on Zn anode after only 10 min deposition, and it becomes more and more fiercer in the following stage in the cells using pristine GF (Figure 3b and 3c). In contrast, during the whole deposition process in the cell using the Cu(II)-PDA/GF separator, the Zn anode maintains smooth without any obvious bulky protuberance, demonstrating superior effect on the inhibition of dendrite growth (Figure 3d-f). The effect may be attributed to the abundant functional groups on PDA, which could induce the transportation of Zn^{2+} at the electrode/electrolyte interface. Notably, the EDS mapping images (Figure S3) of the Zn anode after 10 min deposition presents even distribution of elements Cu, C, N and O, indicating that the Cu(II)-PDA modification layer endows the separator with good adhesion with Zn anode.

XPS measurements of the Cu(II)-PDA/GF separator and Zn anode before and after1h deposition at the current density of 1 mA cm^{-2} in symmetric cells are carried out. As shown in Figure 3g, the intensity of Cu(II) in the Cu(II)-PDA/GF separator sharply decreases after the deposition process. Notably, metal Cu can be obviously detected on the surface of Zn foil, indicating that Cu(II) in the modification layer is transferred into Cu(0) and deposited on Zn anode during the deposition process. It is reported that metallic Cu has a strong Zn binding ability, and can effectively reduce the nucleation overpotential of zinc, thereby promoting uniform deposition of Zn^{2+}, and significantly reducing the possibility of tiny protrusions growing into zinc dendrites [37, 38] (Figure 3g). Therefore, it is believed that the resulted Cu(0) also contributes to the uniform Zn deposition in the cells using Cu(II)-PDA/GF separator.

Preprints (www.preprints.org) | NOT PEER-REVIEWED | Posted: 9 June 2023 doi:10.20944/preprints202306.0719.v1

To evaluate the corrosion current density, Tafel measurements were performed. As shown in Figure 3h, the Cu(II)-PDA/GF separator displays much lower corrosion current density (0.4262 mA cm^{-2}) compared with pristine GF separator (1.1038 mA cm^{-2}), evidence of reduced corrosion level. To further evaluate the hydrophilic character of the separators, a simple water absorption test was carried out. As shown in Figure 3i and Table S1, the Cu(II)-PDA/GF separator has greater water absorption capacity than pristine GF, indicating improved affinity with electrolyte. The Cu(II)-PDA/GF separator with good hydrophilicity and ionic conductivity is expected to guarantee convenient Zn^{2+} transportation of ZIBs during the charge/discharge process.

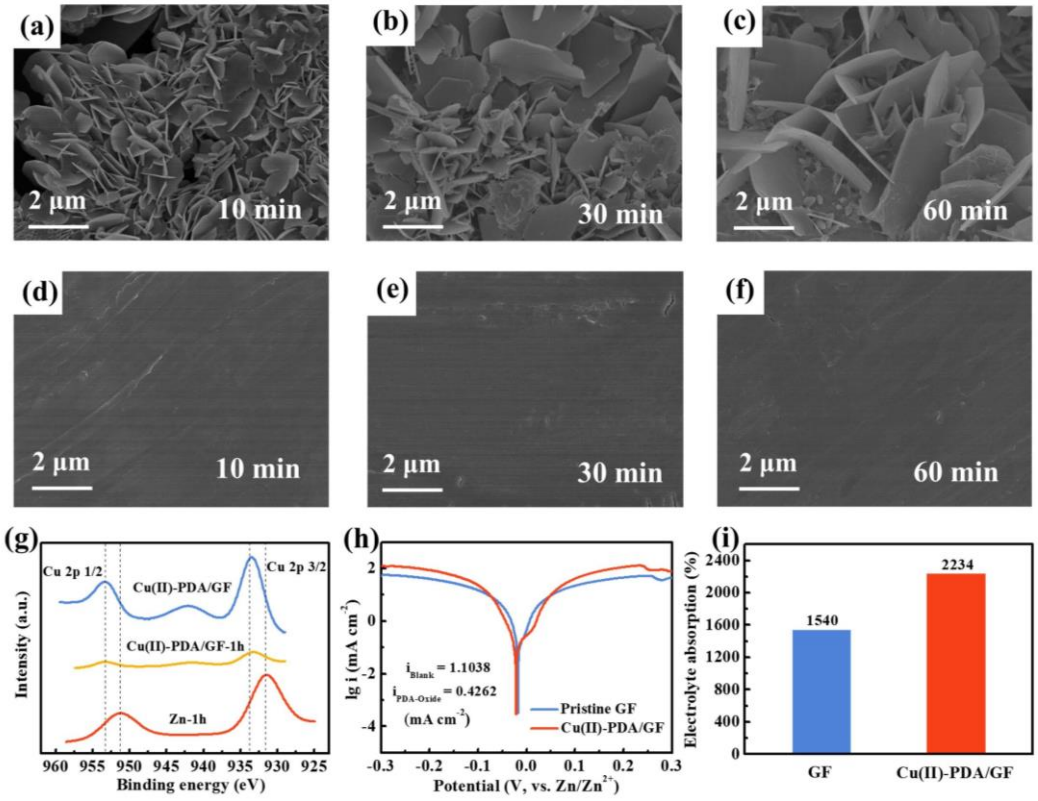

Figure 3. The SEM images of zinc foils after zinc deposition for 10, 30, and 60 min at 1 mA cm^{-2}. (a–c) In pristine GF separator cell. (d–f) In Cu(II)-PDA/GF separator cell. (g) XPS survey spectra of Cu(II)-PDA/GF separator, Cu(II)-PDA/GF separator after 1 h of Zn deposition 1h. (h) Linear polarization curves in pristine GF separator and Cu(II)-PDA/GF separator. (i) Electrolyte absorption of pristine GF separator and Cu(II)-PDA/GF separators with 2 M $ZnSO_4$.

To further evaluate the practical application of the as-prepared Cu(II)-PDA/GF separator, CE tests are carried out in Cu//Zn cells. As shown in Figure 4a and S4, the cells with the Cu(II)-PDA/GF separator displays long cycle life of more than 1200 h and high average CE of 99.62% and 99.81% at the current densities of 1 mA cm^{-2} and 2 mA cm^{-2}, respectively. While the cells employing pristine GF separator (Figure 4a) presents the average CE of 96.2% during the initial 150 h and the CE values fluctuate dramatically in the following cycles. The severe fluctuations mainly result from zinc dendritic growth, parasitic side reactions, and the recovery of "dead Zn" that broke away from hydrated zinc hydroxide sulfate.

From the initial Galvanostatic charge-discharge (GCD) curves of Cu//Zn cells, the nucleation overpotential for Zn deposition can be calculated. The lower nucleation overpotential of the cell indicates that the crystal nucleation barrier is smaller, which is favorable for the uniform deposition and exfoliation of zinc. Otherwise, during the nucleation process of crystal, the nucleation overpo-

Preprints (www.preprints.org) | NOT PEER-REVIEWED | Posted: 9 June 2023 doi:10.20944/preprints202306.0719.v1

tential is large, and the resistance becomes larger [10]. As shown in Figure 4b, the nucleation overpotential of the glass fiber separator battery is 46.24 mV, which is higher than that of the Cu(II)-PDA modified glass fiber separator battery (32.15 mV), indicating that the Cu(II)-PDA/GF separator can promote the uniform deposition of zinc ions. The GCD curves of the Cu//Zn battery with the dopamine-modified separator at the 200th and 500th cycles are very consistent, and also very close to the GCD curve at the 50th cycle. The battery exhibited excellent reversibility with a low voltage difference of 36.0 mV (Figure 4c). However, when the blank separator is used, the overlap of the GCD curves is not very good, and at the same time, the voltage gap is comparatively large (Figure S6).

The cyclic life and overall voltage hysteresis of Zn//Zn symmetric cells using 2 M $ZnSO_4$ as electrolyte is investigated. As shown in Figure 4d, the cell employing Cu(II)-PDA/GF separator exhibits constant voltage profile and delivers favorable cycle life of 1800 h at the current density of 1 mA cm^{-2} with the fixed capacity of 1 mAh cm^{-2}. In contrast, the parallel tested cell with pristine GF suffers quick cell failure after only 95 h due to short-circuiting, which results from the pierce of GF by unrestrained growth of dendrites. Enlarged GCD curves displays decreased voltage hysteresis for the cell with Cu(II)-PDA/GF separator, indicating improved ion transportation ability. The cells using Cu(II)-PDA/GF separator also deliver stable plating/striping of 430 h at increased current density of 2 mA cm^{-2} and areal capacity of 2 mAh cm^{-2} (Figure S6), and 260 h at an higher current density of 4 mA cm^{-2} and 4 mAh cm^{-2} (Figure 4e), which are much superior to those suing pristine GF separator.

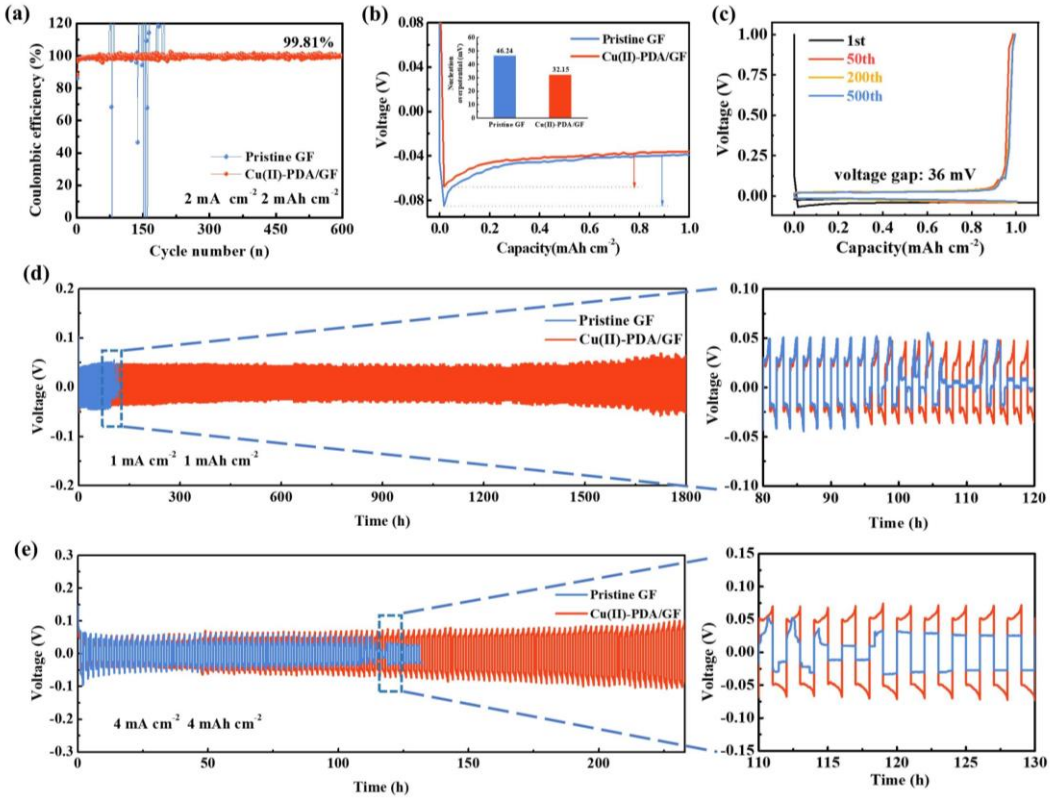

Figure 4. (a) Columbic efficiency of plating/stripping Zn on Cu at the current density of 1 mA cm^{-2} with the fixed capacity of 1 mAh cm^{-2} in Cu//Zn cells; (b) First-week voltage capacity distribution of Cu//Zn cells with pristine GF and Cu(II)-PDA/GF separator (nucleation overpotential values shown in the inset); (c) Voltage and capacity distribution of Cu//Zn cells with Cu(II)-PDA/GF separator assembled for different cycles; Cycling performance in symmetrical cells with pristine GF and Cu(II)-PDA/GF separator at the current density of (d) 1 mA cm^{-2} and (e) 4 mA cm^{-2}.

The morphology evolution of the Zn anode after 50 cycles in the symmetric cells using pristine separator and Cu(II)-PDA/GF separator was characterized by SEM. As shown in Figure 5a and 5b, the cycled Zn anode of the cell with the modified separator presents a relatively flat surface without

Preprints (www.preprints.org) | NOT PEER-REVIEWED | Posted: 9 June 2023 doi:10.20944/preprints202306.0719.v1

obvious zinc dendrites, and the SEM images of the cross-section (Figure 5c) also exhibits smooth surface without passivation layer. While the Zn anode in the cell using the pristine separator (Figure 5d and 5e) displays serious zinc dendrite growth, and the surface of Zn anode is full of vertically grown microsheets, which may pierce the separator. SEM image of the cross-section (Figure 5f) also shows a non-uniform corrosion layer. Therefore, it is confirmed that the Cu(II)-PDA/GF separator could inhibit the dendrite growth and chemical corrosion effectively, which can also be confirmed by reduced R_{ct} in the EIS tests (Figure 5g and 5h). In order to obtain more phase information, XRD patterns of the Zn anodes after 50 cycles in the cells with different separators were measured (Figure 5i). Obviously, characteristic peaks of $Zn_4SO_4(OH)_6{\cdot}5H_2O$ are visible in the XRD pattern of the Zn anode using pristine GF [39], illustrating that side reactions easily take place on the Zn anode and produce massive by-products during cycling. In contrast, the peak intensity of by-produces is significantly decreased when using Cu(II)-PDA/GF separator, further illustrating that the modified GF separator could effectively prevent the electrode passivation.

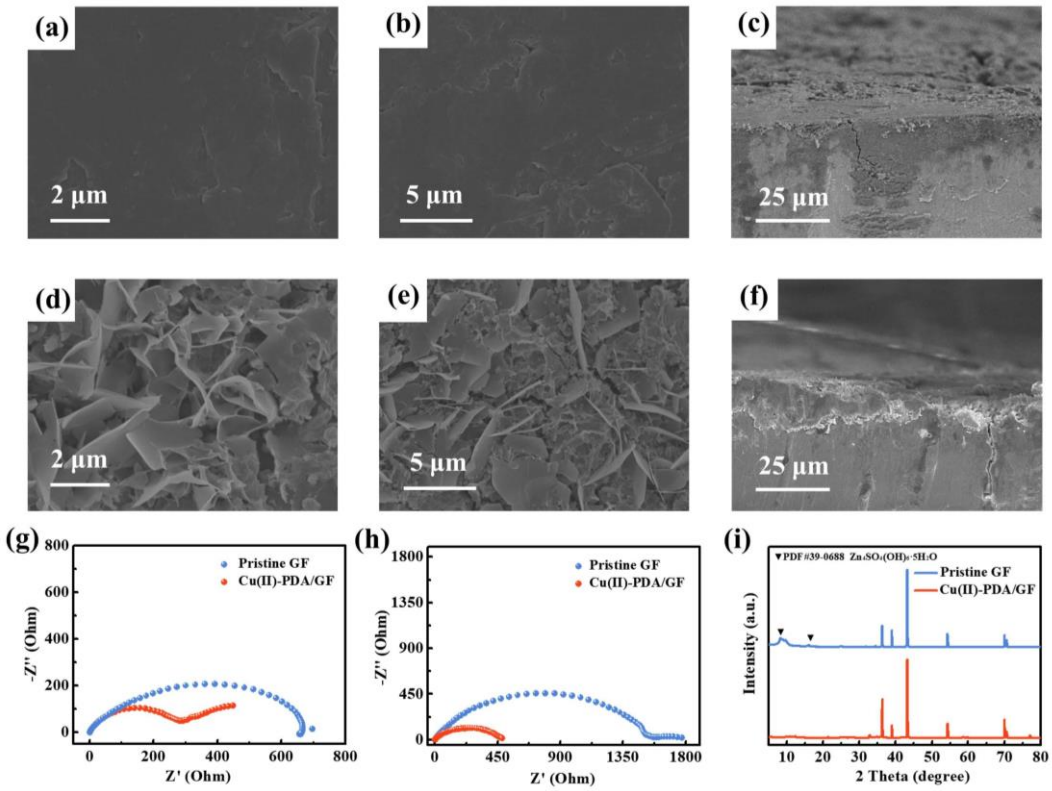

Figure 5. Surface morphology and cross-sectional SEM images of the Zn anode after 50 cycles at 1 mA cm^{-2} and 1 mAh cm^{-2} in the cells using (a–c) Cu(II)-PDA/GF separator and (d–f) pristine GF separator. The EIS spectra of the symmetric cells using different separators (g) before cycling and (h) after 50 cycles; (i) XRD patterns of the Zn anode after 50 cycles at 1 mA cm^{-2} and 1 mAh cm^{-2} with pristine GF and Cu(II)-PDA/GF separator.

In order to evaluate the practical performance of the modified separator, Zn//V_2O_5 full cells were assembled to study the electrochemical performance. The CV curve of the cells with Cu(II)-PDA/GF separator displays two pairs of redox peaks (Figure 6a), indicating that intercalation/deintercalation behavior of Zn ion in V_2O_5 were carried out in two steps. After three cycles, it could be found that the redox peaks overlap well, indicating the superior cycling reversibility of the full cells with Cu(II)-PDA/GF separator.

Rate capability of the full cells are shown in Figure 5b. It can be seen that when the current density gradually increases from 0.2 to 0.5, 1.0 and 2.0, the battery assembled with the Cu(II)-PDA/GF separator decreased from 281.0 to 276.0, 265.3 and 240.6 mAh g^{-1}, respectively. In contrast, the battery

Preprints (www.preprints.org) | NOT PEER-REVIEWED | Posted: 9 June 2023 doi:10.20944/preprints202306.0719.v1

assembled with the pristine separator (Figure 6b) maintained 213.7 mAh g^{-1} at 0.2 A g^{-1}, and dropped abruptly to 192.4 mAh g^{-1} at 2 A g^{-1}. Notably, when the current density was returned from 2 to 0.2 A g^{-1}, the battery with the Cu(II)-PDA/GF separator could provide 258.8 mAh g^{-1} at the 70th, which is much higher than that using glass fiber separator.

Cycling performance of the cells was tested with constant current charge and discharge density. GCD curves display two pairs of reversible voltage platforms, which are consistent with the CV results (Figure 6c). After 1000 cycles at a current density of 2 A g^{-1}, the battery assembled with Cu(II)-PDA/GF delivers a high capacity of 202.3 mAh g^{-1}, which is much higher than that of 146.2 mAh g^{-1} using pristine separator (Figure 6d). Moreover, the CE value of the Cu(II)-PDA/GF separator keeps steady and nearly 100% after long term cycling, displaying the significant improvement of the full cell performance.

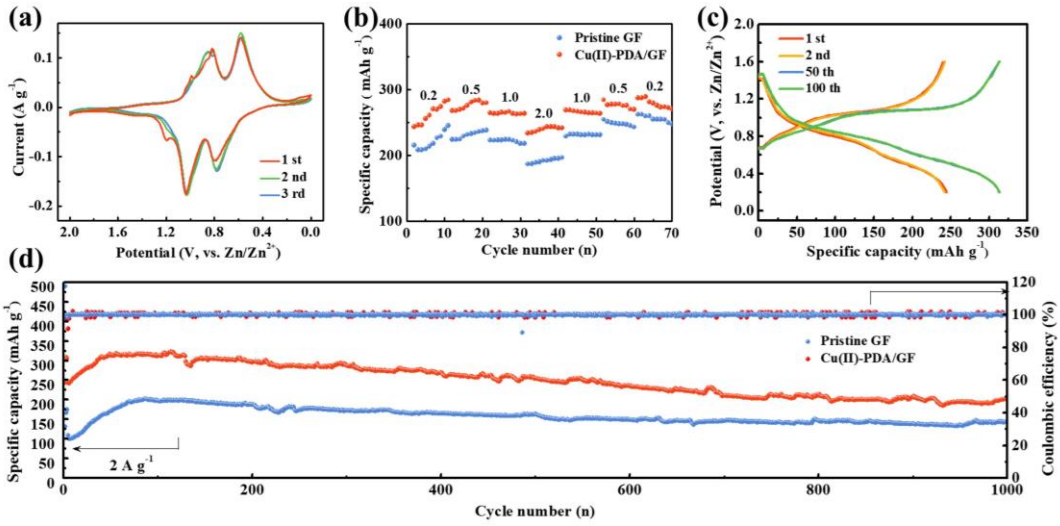

Figure 6. Electrochemical properties of the Zn/V_2O_5 full cells: (a) CV curves measured at a scan rate of 0.05 mV s^{-1}; (b) Rate performance measured from 0.2 to 2 A g^{-1}; (c) 1st, 2nd, 50th and 100th discharge/charge curves of the full cells with Cu(II)-PDA/GF separator; (d) Cycling performance of the full cells at a current density of 2 A g^{-1}.

4. Conclusions

In summary, PDA nano-polymer is self-assembled on the surface of glass fiber via a self-polymerization process to obtain Cu(II)-PDA/GF separator. The modification of PDA effectively improves the zincophile and ion transport of GF separator. Cu(II) doping in the PDA coating layer could be preferentially deposited on Zn anode to induce uniform Zn nucleation. Due to the synergistic effect, side reactions and dendrite growth of Zn anode are effectively depressed. Electrochemical measurements demonstrate that the symmetric cells assembled with Cu(II)-PDA/GF separator could cycle for more than 1800 h at the current density of 1.0 mA cm^{-2} with the fixed capacity of 1.0 mAh cm^{-2}. The Zn//V_2O_5 cells using the modified GF also deliver high specific capacity and good cycling stability of 202.3 mAh g^{-1} after 1000 cycles at 2.0 A g^{-1}. This work provides a facile modification method for glass fiber for high-performance ZIBs.

Acknowledgments: This work was supported by the Natural Science Foundation of Jiangsu Province (No. BK20211352), Natural Science Foundation of Jiangsu Education Committee of China (No. 22KJA430005).

References

1. Huang, Y.; Zhu, M.; Huang, Y.; Pei, Z.; Li, H.; Wang, Z.; Xue, Q.; Zhi, C. Multifunctional Energy Storage and Conversion Devices. *Adv. Mater.* **2016**, *28*, 8344-8364.

2. Li, C.; Jin, S.; Archer, L.A.; Nazar, L.F. Toward practical aqueous zinc-ion batteries for electrochemical energy storage. *Joule* **2022**, *6*, 1733-1738.
3. Kittner, N.; Lill, F.; Kammen, D.M. Energy storage deployment and innovation for the clean energy transition. *Nature Energy* **2017**, *2*, 1-6.
4. Dong, L.; Yang, W.; Yang, W.; Li, Y.; Wu, W.; Wang, G. Multivalent metal ion hybrid capacitors: a review with a focus on zinc-ion hybrid capacitors. *J. Mater. Chem. A* **2019**, 7, 13810-13832.
5. Pan, Z.; Liu, X.; Yang, J.; Li, X.; Liu, Z.; Loh, X.; Wang, J. Aqueous Rechargeable Multivalent Metal-Ion Batteries: Advances and Challenges. *Adv. Energy Mater.***2021**, *11*, 2100608.
6. Liang, Y.; Dong, H.; Aurbach, D.; Yao, Y. Current status and future directions of multivalent metal-ion batteries. *Nature Energy* **2020**, *5*, 646-656.
7. Dunn, B.; Kamath, H.; Tarascon, J.-M. Electrical Energy Storage for the Grid: A Battery of Choices. *Science* **2011**, *334*, 928-935.
8. Huang, J.; Guo, Z.; Ma, Y.; Bin, D.; Wang, Y.; Xia, Y. Recent Progress of Rechargeable Batteries Using Mild Aqueous Electrolytes. *Small Methods* **2019**, 3, 1800272.
9. Wang, K.; Pei, P.; Ma, Z.; Chen, H.; Xu, H.; Chen, D.; Wang, X. Dendrite growth in the recharging process of zinc-air batteries. *J. Mater. Chem. A* **2015**, *3*, 22648-22655.
10. Zhou, W.; Chen, M.; Tian, Q.; Chen, J.; Xu, X.; Wong, C.-P. Cotton-derived cellulose film as a dendrite-inhibiting separator to stabilize the zinc metal anode of aqueous zinc ion batteries. *Energy Stor. Mater.* **2022**, *44*, 57-65.
11. Hopkins, B.J.; Sassin, M.B.; Chervin, C.N.; Desario, P.A.; Parker, J.F.; Long, J.W.; Rolison, D.R. Fabricating architected zinc electrodes with unprecedented volumetric capacity in rechargeable alkaline cells. *Energy Stor. Mater.* **2020**, *27*, 370-376.
12. Wang, Y.; Liu, Y.; Wang, H.; Dou, S.; Gan, W.; Ci, L.; Huang, Y.; Yuan, Q. MOF-based ionic sieve interphase for regulated Zn^{2+} flux toward dendrite-free aqueous zinc-ion batteries. *J. Mater. Chem. A* **2022**, *10*, 366-4375.
13. Han, D.; Ma, T.; Sun, T.-J.; Zhang, W.-J.; Tao, Z.-L. Zinc Anode Protection Strategy for Aqueous Zinc-Ion Batteries. *Chinese J. Inorg. Chem.* **2022**, *38*, 185-197.
14. Yu, Y.; Xu, W.; Liu, X.; Lu, X. Challenges and Strategies for Constructing Highly Reversible Zinc Anodes in Aqueous Zinc-Ion Batteries: Recent Progress and Future Perspectives. *Adv. Sustain. Syst.* **2020**, *4*, 2000082.
15. Zhang, Q.; Luan, J.; Tang, Y.; Ji, X.; Wang, H. Interfacial Design of Dendrite-Free Zinc Anodes for Aqueous Zinc-Ion Batteries. *Angew. Chem. Int. Ed.* **2020**, *59*, 13180-13191.
16. Han, C.; Li, W.; Liu, H.K.; Dou, S.; Wang, J. Principals and strategies for constructing a highly reversible zinc metal anode in aqueous batteries. *Nano Energy* **2020**, *74*, 104880.
17. Yi, Z.; Chen, G.; Hou, F.; Wang, L.; Liang, J. Strategies for the Stabilization of Zn Metal Anodes for Zn-Ion Batteries. *Adv. Energy Mater.* **2021**, *11*, 2003065.
18. Guo, X.; Zhang, Z.; Li, J.; Luo, N.; Chai, G.-L.; Miller, T.S.; Lai, F.; Shearing, P.; Brett, D.J.L.; Han, D.; Weng, Z.; He, G.; Parkin, I.P. Alleviation of Dendrite Formation on Zinc Anodes via Electrolyte Additives. *ACS Energy Lett.* **2021**, *6*, 395-403.
19. Du, Y.; Li, Y.; Xu, B.B.; Liu, T.X.; Liu, X.; Ma, F.; Gu, X.; Lai, C. Electrolyte Salts and Additives Regulation Enables High Performance Aqueous Zinc Ion Batteries: A Mini Review. *Small* **2021**, *18*, 2104640.
20. Abdulla, J.; Cao, J.; Zhang, D.; Zhang, X.; Sriprachuabwong, C.; Kheawhom, S.; Wangyao, P.; Qin, J. Elimination of Zinc Dendrites by Graphene Oxide Electrolyte Additive for Zinc-Ion Batteries. *ACS Appl. Energy Mater.* **2021**, *4*, 4602-4609.
21. Guo, S.; Qin, L.; Zhang, T.; Zhou, M.; Zhou, J.; Fang, G.; Liang, S. Fundamentals and perspectives of electrolyte additives for aqueous zinc-ion batteries. *Energy Stor. Mater.* **2021**, *34*, 545-562.
22. Wu, K.; Huang, J.; Yi, J.; Liu, X.; Liu, Y.; Wang, Y.; Zhang, J.; Xia, Y. Recent Advances in Polymer Electrolytes for Zinc Ion Batteries: Mechanisms, Properties, and Perspectives. *Adv. Energy Mater.* **2020**, *10*, 1903977.
23. Lu, K.; Jiang, T.; Hu, H.; Wu, M. Hydrogel Electrolytes for Quasi-Solid Zinc-Based Batteries. *Front. Chem.* **2020**, *8*, 546728.
24. Li, X.; Wang, D.; Ran, F. Key approaches and challenges in fabricating advanced flexible zinc-ion batteries with functional hydrogel electrolytes. *Energy Stor. Mater.* **2023**, *56*, 351-393.
25. Dong, H.; Li, J.; Guo, J.; Lai, F.; Zhao, F.; Jiao, Y.; Brett, D.J.L.; Liu, T.; He, G.; Parkin, I.P. Insights on Flexible Zinc-Ion Batteries from Lab Research to Commercialization. *Adv. Mater.* **2021**, *33*, 2007548.

26. Liu, D.; Tang, Z.; Luo, L.; Yang, W.; Liu, Y.; Shen, Z.; Fan, X.-H. Self-Healing Solid Polymer Electrolyte with High Ion Conductivity and Super Stretchability for All-Solid Zinc-Ion Batteries. *ACS Appl. Mater. Interfaces* **2021**, *13*, 36320-36329.
27. Li, C.; Sun, Z.; Yang, T.; Yu, L.; Wei, N.; Tian, Z.; Cai, J.; Lv, J.; Shao, Y.; Rummeli, M.H.; Sun, J.; Liu, Z. Directly Grown Vertical Graphene Carpets as Janus Separators toward Stabilized Zn Metal Anodes. *Adv. Mater.* **2020**, *32*, 2003425.
28. Su, Y.; Liu, B.; Zhang, Q.; Peng, J.; Wei, C.; Li, S.; Li, W.; Xue, Z.; Yang, X.; Sun, J. Printing-Scalable $Ti_3C_2T_x$ MXene-Decorated Janus Separator with Expedited Zn^{2+} Flux toward Stabilized Zn Anodes. *Adv. Funct. Mater.* **2022**, *32*, 2204306.
29. Liu, T.; Hong, J.; Wang, J.; Xu, Y.; Wang, Y. Uniform distribution of zinc ions achieved by functional supramolecules for stable zinc metal anode with long cycling lifespan. *Energy Stor. Mater.* **2022**, *45*, 1074-1083.
30. Cao, J.; Zhang, D.; Gu, C.; Wang, X.; Wang, S.; Zhang, X.; Qin, J.; Wu, Z.-S. Manipulating Crystallographic Orientation of Zinc Deposition for Dendrite-free Zinc Ion Batteries. *Adv. Energy Mater.* **2021**, *11*, 2101299.
31. Ryou, M.-H.; Lee, D.J.; Lee, J.-N.; Lee, Y.M.; Park, J.-K.; Choi, J.W. Excellent Cycle Life of Lithium-Metal Anodes in Lithium-Ion Batteries with Mussel-Inspired Polydopamine-Coated Separators. *Adv. Energy Mater.* **2012**, *2*, 645-650.
32. Shi, X.; Xu, G.; Liang, S.; Li, C.; Guo, S.; Xie, X.; Ma, X.; Zhou, J. Homogeneous Deposition of Zinc on Three-Dimensional Porous Copper Foam as a Superior Zinc Metal Anode. *ACS Sustain. Chem. Eng.* **2019**, *7*, 17737-17746.
33. Qian, Y.; Meng, C.; He, J.; Dong, X. A lightweight 3D Zn@Cu nanosheets@activated carbon cloth as long-life anode with large capacity for flexible zinc ion batteries. *J. Power Sources* **2020**, *480*, 228871.
34. Li, C.; Shi, X.; Liang, S.; Ma, X.; Han, M.; Wu, X.; Zhou, J. Spatially homogeneous copper foam as surface dendrite-free host for zinc metal anode. *Chem. Eng. J.* **2020**, *379*, 122248.
35. Zhang, C.; Ou, Y.; Lei, W.-X.; Wan, L.-S.; Ji, J.; Xu, Z.-K. $CuSO_4/H_2O_2$-Induced Rapid Deposition of Polydopamine Coatings with High Uniformity and Enhanced Stability. *Angew. Chem. Int. Ed.* **2016**, *55*, 3054-3057.
36. Yu, F.; Chen, S.; Chen, Y.; Li, H.; Yang, L.; Chen, Y.; Yin, Y. Experimental and theoretical analysis of polymerization reaction process on the polydopamine membranes and its corrosion protection properties for 304 Stainless Steel. *J. Mol. Struct.* **2010**, *982*, 152-161.
37. Zeng, Y.; Sun, P.X.; Pei, Z.; Jin, Q.; Zhang, X.; Yu, L.; Lou, X.W. Nitrogen-Doped Carbon Fibers Embedded with Zincophilic Cu Nanoboxes for Stable Zn-Metal Anodes. *Adv. Mater.* **2022**, *34*, 2200342.
38. Xie, S.; Li, Y.; Li, X.; Zhou, Y.; Dang, Z.; Rong, J.; Dong, L. Stable Zinc Anodes Enabled by Zincophilic Cu Nanowire Networks. *Nanomicro Lett* **2022**, *14*, 39.
39. Lu, H.; Zhang, X.; Luo, M.; Cao, K.; Lu, Y.; Xu, B.B.; Pan, H.; Tao, K.; Jiang, Y. Amino Acid-Induced Interface Charge Engineering Enables Highly Reversible Zn Anode. *Adv. Funct. Mater.* **2021**, *31*, 2103514.